

Effect of the particle size on the thermal stability of nanostructured aluminum powder: dislocation density and second-phase particles controlling the grain growth

A. Molinari · I. Lonardelli · K. Demetrio · C. Menapace

Received: 10 December 2009 / Accepted: 13 July 2010 / Published online: 27 July 2010
© Springer Science+Business Media, LLC 2010

Abstract A nanostructured aluminum powder was obtained using cryogenic mechanical milling. The powder produced after 25 h of milling showed a broad particle size distribution, ranging between a few microns up to about 150 µm. Five different granulometric classes were selected and for each of these, structural and microstructural features, as well as the thermal stability were investigated using ex situ X-ray diffraction and transmission electron microscopy. There is a direct correlation between particle size and crystallite size. Grain growth tendency was found strongly dependent to the initial grain size with noticeable changes on the thermal stability for the five granulometric classes considered. Particularly the quantity of nitrogen content measured (after degassing) in each of the five granulometric classes increases with decreasing the particles size. This might justify why the calculated drag stress exerted by segregated impurities, second-phase particles and pores is effectively higher for small particles. This approach can give a methodology to modulate the microstructure of bulk nanostructured/ultrafine metals just selecting different combination in terms of particle size.

Introduction

Bulk nanocrystalline aluminum can be produced by cryomilling of powders [1, 2] and their consolidation by Spark Plasma Sintering [3]. As well known, the mechanical properties are characterized by an increasing yield stress on

decreasing grain size, coupled to a low ductility because of the poor strain hardenability of the nanostructured materials [4–6].

However, ductility can be significantly increased by a bimodal distribution of the grain size [7, 8].

The control of the grain size distribution during consolidation processes is then of paramount importance to achieve the desired mechanical properties of a nanocrystalline material.

In general, the thermal stability of a microstructure will depend on the lattice defects stored within and between grains and on the particles (oxides and nitrides) due to either dispersion or precipitation of a second-phase from a solid solution. Particularly, for nanocrystalline materials, impurities segregated at the grain boundary, nanoporosity and nanoparticles either “pinned” at the grain boundary must be considered as strong stabilizers for the nanostructure.

In the case of aluminum milled in the liquid nitrogen it was shown the presence of the Al-bearing dispersoids (AlN , Al(O)N or Al_2O_3) adjacent to the grain boundary [9] that act as particles drag (Zener drag, [10, 11]). These particles provide a pinning force that would not be present in the mechanically milled Fe powder [12–14].

However, the study of the thermal stability in cryomilled aluminum related either to the lattice defects stored after milling and to the formation of AlN or Al -oxide at the grain boundary has not been investigated to a great extent.

The present work proposes a study of the thermal stability of nanostructured aluminum powder obtained after cryomilling process considering five different granulometric classes. Both the dislocation density contribution and the solute segregation contribution against grain boundary motion are discussed and related to the experimental results.

A. Molinari · I. Lonardelli (✉) · K. Demetrio · C. Menapace
Department of Materials Engineering and Industrial
Technologies, University of Trento, 38050 Trento, Italy
e-mail: ivan.lonardelli@ing.unitn.it

Experimental procedure

Samples of nanocrystalline (nc) Al were produced by mechanical milling of a slurry of aluminum powders and liquid nitrogen, a process known as cryomilling. Elemental powder of pure aluminum (average particle size 200 µm, 99.8%) was used as raw material. The milling was performed in a modified Union Process 01-HD attritor with a stainless steel vial at a rate of 300 rotation per minute (rpm) for a total milling time of 25 h. Stainless steel balls (6.4 mm diameter) were used with a ball to powder ratio of 32:1. During the milling operation, liquid nitrogen was added directly into the stainless steel vial to maintain complete immersion of the milling media. Liquid nitrogen was used also as lubricant without any process control agent (PCA) added.

The cryomilled powder was sieved into five granulometric fractions, heat treated in high vacuum (10^{-5} Torr) at three different temperatures (350, 450, and 550 °C) and analyzed using X-ray diffraction technique (XRD). For each granulometric fraction the diffraction pattern was collected using a Cu $\text{k}\alpha$ ($\lambda = 1.5418$) source and an image plate detector over the 2θ range from 10° to 100° in reflection geometry. The experimental spectra were elaborated with the Rietveld method using the materials analysis using diffraction (MAUD) software [15–17]. Line profile analysis was performed using Popa approach [18] incorporated into the Rietveld algorithm to account the possible anisotropy of the crystallite shape and microstrain. However, the crystallite size (D) and the microstrain ($\langle \varepsilon^2 \rangle^{1/2}$) values did not reveal any major anisotropy. For this reason,

as will be shown in the next section, only the average of the domain size and the microstrain will be reported.

The granulometric fractions were characterized in terms of the nitrogen content after degassing at 350 °C to remove the molecular nitrogen and oxygen adsorbed on the surface of the particles.

The powders were then consolidated in a DR. SINTER 1050® SPS system (Sumitomo Coal & Mining Ltd.) apparatus using a graphite die. SPS was carried out at 600 °C with 2 min isothermal holding at the maximum temperature. Heating rate was 100 °C/min and the pressure applied was 60 MPa.

Transmission electron microscopy (TEM) observations were performed on the sintered samples using a Philips CM12 microscope operating at 120 kV to investigate the presence of dispersoids eventually formed during SPS from the solid solution. TEM foils (disks 3 mm in diameter) were mechanically ground to a thickness of about 70 µm and then ion milled to electron transparency using 6-kV Ar^+ ions and a thinning angle of 15°.

Results and discussion

Characterization of the as-milled powder

The cryo-milled powder was sieved into five different granulometric fractions (<25, 25–45, 45–90, 90–120, and >120 µm) showing a particle size distribution over a broad range, from few micrometers up to around 150 µm (Fig. 1).

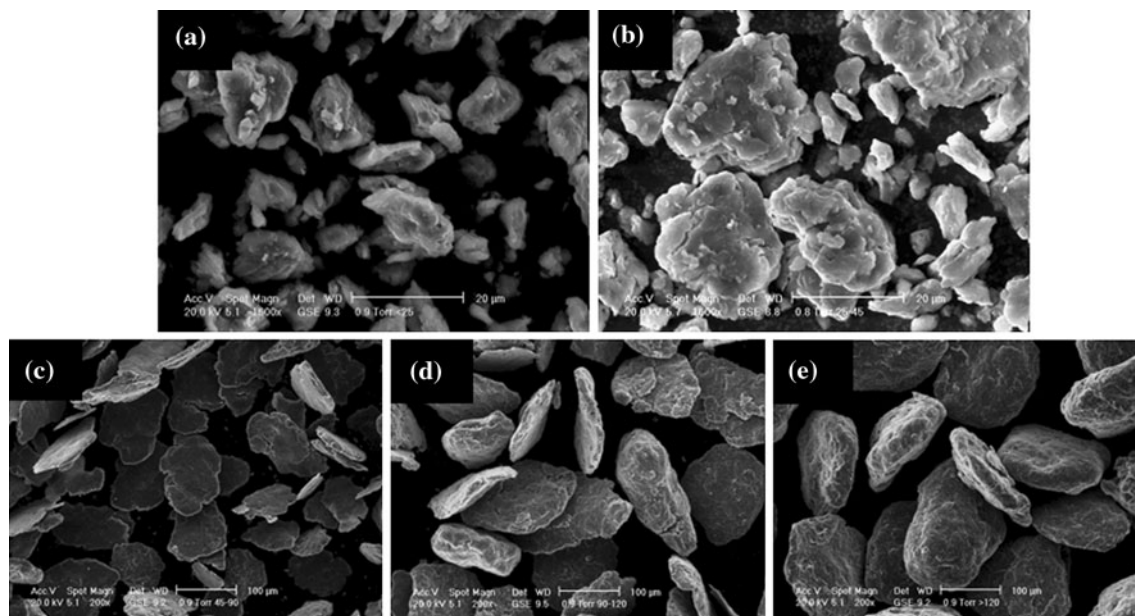


Fig. 1 SEM micrographs of the five granulometric classes for Al powder after 25 h of cryomilling. The five different granulometric classes, with the particle size less than 25 µm (a), 45 µm (b), 90 µm (c), 120 µm (d), and 180 µm (e), were separated after sieving for 1 h using vibratory mill

Figure 2a and b show a bright field (BF) and a dark field (DF) TEM images and the selected area electron diffraction (SAED) pattern of the cryomilled powder (particle size $<25 \mu\text{m}$, 25 h milling time) in which some nanometric grains are clearly identified. Three of them pointed by arrows are measured (average length) using the DF image. We observe a broad distribution of the grain size (here the size varies between 27 and 62 nm) where only few grains approach the minimum grain size that is obtainable by milling. Average crystallite size and microstrain (%) for each granulometric class were determined using XRD technique. The experimental spectra and the results are reported in Fig. 3 and Table 1, respectively. The diffraction peaks are broader in finer particles resulting in a smaller crystallite size and in a larger amount of microstrain. There is a minimum value of the crystallite size that can be reached by ball milling. It depends to the intrinsic properties of the material (crystal structure) as suggested by experimental and theoretical studies [19]. A recent dislocation model was proposed by Mohamed [20] in which the minimum grain size is governed by a balance between the hardening rate introduced by dislocation generation and the recovery rate arising from dislocation annihilation and polygonization. The model suggests proportionality between the minimum grain size and stacking fault energy and an exponential dependence with the activation energy for recovery. For pure aluminum, the minimum crystallite size attainable by ball milling is around 22 nm [20], and is not expected to further decrease by cryomilling. This is reasonably due to the high stacking fault energy and low activation energy for the recovery of this metal. As a confirmation, Zhou et al. [2, 13] report a mean crystallite size of 26 nm on a cryomilled Al powder, and an isotropic microstrain of 0.15% similar to that

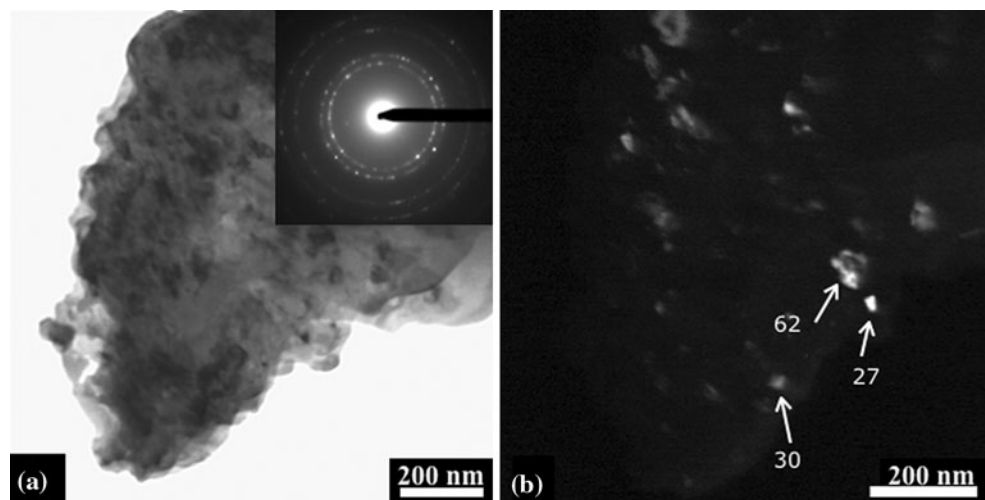


Fig. 2 TEM micrographs of Al powder after milling (25 h) in liquid nitrogen medium. Bright field (a) and dark field (b) show nanometric grains. The grain size is broad distributed (see *dark field picture*) ranging between 27 and 65 nm

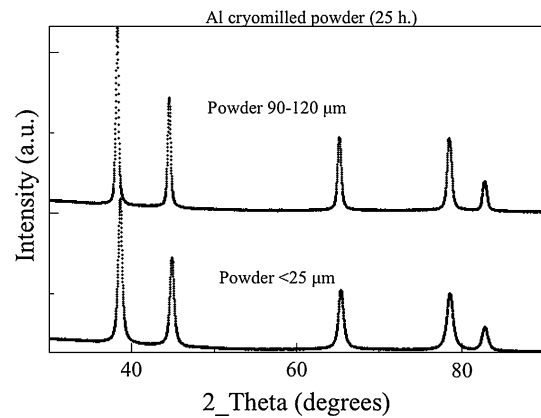


Fig. 3 Diffraction spectra of the milled Al powder (25 h) for two different granulometric classes. Note the difference of the peaks broadening

Table 1 Crystallite size D and microstrain $\langle \varepsilon^2 \rangle^{1/2}$ of the five granulometric fractions

Granulometric class (μm)	D (nm)	$\langle \varepsilon^2 \rangle^{1/2}$ (%)
<25	35 (1)	0.221 (10)
25–45	48 (2)	0.172 (11)
45–90	80 (3)	0.125 (13)
90–120	108 (6)	0.097 (11)
>120	119 (6)	0.087 (12)

The values of standard deviation are from the Rietveld refinement

reported by Eckert and co-workers on a ball milled Al powder [19]. The minimum crystallite size obtained here is significant larger and the corresponding mean lattice strain is higher suggesting that the microstructure is still under refinement even in the volume fraction with the finer

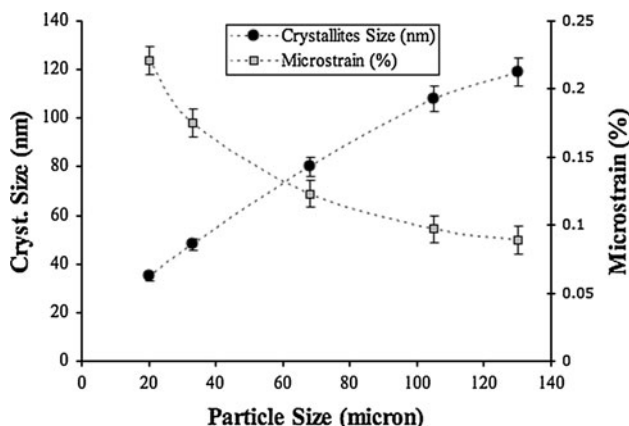


Fig. 4 Crystallite size and microstrain changes as a function of the mean particle size for the five granulometric fractions

particles. Figure 4, shows the crystallite size and the microstrain as a function of the mean particle size. The results suggest huge microstructural differences between particles processed using the same milling time.

The inverse correlation between crystallite size and microstrain was studied and discussed in [21, 22].

Tian and Atzon [22] carried out low energy milling experiments on pure iron, under different vibration amplitudes and milling times. Grain size decreases and microstrain increases with milling time, both reaching a steady state. They also report a linear relationship between $\langle \varepsilon^2 \rangle^{1/2}$ and D^{-1} in a size range below 40 nm. Figure 5 shows the plot of $\langle \varepsilon^2 \rangle^{1/2}$ versus D^{-1} for the five granulometric fractions investigated here. Despite the limited number of experimental data, it can be observed that points representative to the large crystallite size deviate slightly from the linear trend. This is due to the low sensitivity of XRD in measuring crystallite size when they are approaching 150 nm.

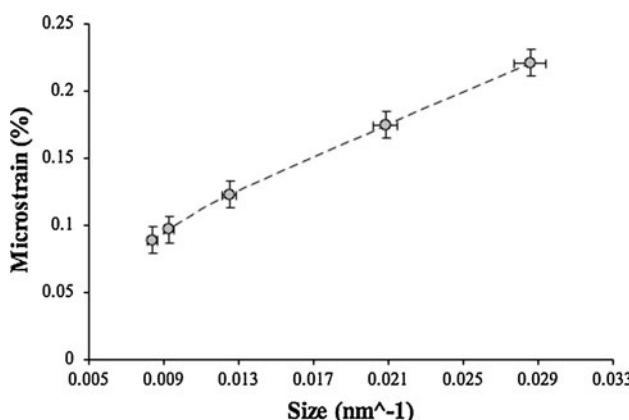


Fig. 5 Microstrain vs. the reciprocal of crystallite size for the five granulometric fractions

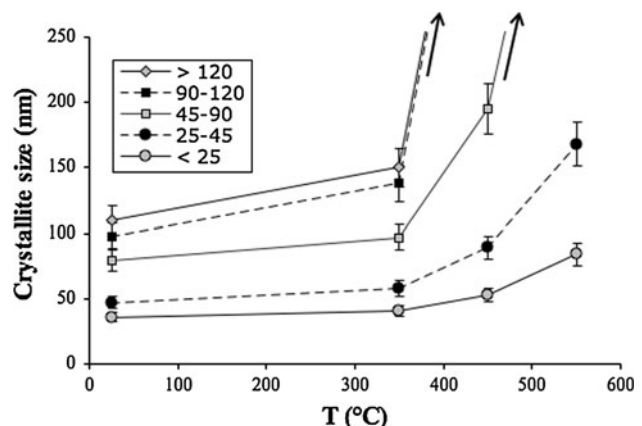


Fig. 6 Grain growth of the five granulometric classes. For each temperature considered (350, 450, and 550 °C) isothermal heat treatments (1 h) were performed. The arrows indicate that for higher temperatures the crystallite size is actually not detectable with XRD technique

Thermal stability and grain growth

Figure 6 shows the mean crystallite size versus annealing temperature (1 h holding) for each granulometric fraction. The grain growth tendency is quite different, and increases with increasing the starting grain size. Particularly:

- grain size of the 35 nm powder is stable up to 350 °C, then it slightly increases but retains the nanocrystalline structure over the whole temperature range investigated (78 nm at 550 °C)
- grain size of the 48 nm powder has the same behavior and still retains the nanocrystalline structure (155 nm at 550 °C)
- grain size of the 80, 108, and 119 behave differently, losing the nanostructure between 350 and 450 °C.

The results indicate that the finer powder (with a smaller average crystallite size) exhibits a strong thermal stability even if the driving force for the grain growth is higher (a lot of interfaces). The thermal stability will be explained in terms of dislocation density and second-phase particles that enhance the pinning force opposing grain growth.

Dislocation density and solute drag

The driving force for the grain growth is the excess of Gibbs free energy correlated to the grain boundary surface, and is expressed by the following equation [14]:

$$\Delta G = \gamma_{gb} \Delta S = 3.3 \gamma_{gb} / D \quad (1)$$

where ΔG is the driving force for grain growth, ΔS is the specific grain boundary surface, D is the crystallite diameter, and γ_{gb} is the specific grain boundary energy [14]. The grain boundary volume fraction increases on decreasing the mean crystallite size then, from a thermodynamic point of

Table 2 Crystallite size (D), dislocation density (ρ), and critical dislocation density (ρ_{cr}) of the milled powder calculated for each granulometric fraction, using two different values of the specific grain boundary energy [28]

Granulometric class (μm)	D (nm)	ρ (m^{-2})	ρ_{cr} (m^{-2}) $\gamma_{\text{gb}} = 0.18 \text{ J/m}^2$	ρ_{cr} (m^{-2}) $\gamma_{\text{gb}} = 0.32 \text{ J/m}^2$
<25	35 (1)	0.74×10^{15}	1.47×10^{15}	4.66×10^{15}
25–45	48 (2)	0.49×10^{15}	0.78×10^{15}	2.48×10^{15}
45–90	80 (3)	0.19×10^{15}	0.28×10^{15}	0.89×10^{15}
90–120	108 (6)	0.10×10^{15}	0.15×10^{15}	0.49×10^{15}
>120	119 (6)	0.08×10^{15}	0.13×10^{15}	0.40×10^{15}

view, the smaller the grain size, the bigger the tendency to grain growth. Grain growth at homologous temperatures below $0.5 T_m$ is however, opposed by lattice defects (dislocations, stacking faults, etc.) that interact each other. The lattice strain in nanostructured powders can be modeled by quantifying the dislocation density [23], with an almost equal fraction of edge and screw types [24].

The average microstrain and domain size determined by XRD analysis using the modified Rietveld method were then transformed in a dislocation density as described in [25]. The average density of dislocation (ρ) has been estimated from the relation $\rho = (\rho_D \rho_S)^{1/2}$, where $\rho_D = 3/D_s^2$ (dislocation density due to the domain size) and $\rho_S = k\langle\varepsilon_L^2\rangle/b^2$ (dislocation density due to the microstrain), k is the material constant, and b is the modulus of the Burger's vector. Table 2 reports the resulting dislocation densities calculated for each granulometric class. The dislocation density ranges between $0.8 \times 10^{14} \text{ m}^{-2}$ and $7.35 \times 10^{14} \text{ m}^{-2}$. These values are compatible to that of a highly deformed aluminum. As observed by Moelle and Fecht [14], the grain boundary mobility is reduced by large strain accumulated in the adjoining regions. This implies that grain size can grow only after a certain amount of strain has been released by recovery.

If grain boundary is described as an array of dislocation, the resistance offered by strain accumulated between and within the grain can be expressed by the stress required to move dislocation against. This approach was used by Chatterjee et al. [26] to study mechanical stabilization of austenite in martensitic transformation, and applied by Molinari et al. [27] to study thermal stability of a nanostructured FeMo alloy. From a micromechanic point of view, it may be assumed that the grain boundary motion is driven by the stress τ_1 resulting from the driving force of grain growth (Eq. 1) and is opposed by the resistance τ_2 , the drag force induced by the dislocations in the strained regions.

The two stresses are given by Eqs. 2 and 3 [26]:

$$\tau_1 = \Phi \Delta G = \Phi \gamma_{\text{gb}} \Delta S = 3.3 \Phi \gamma_{\text{gb}} / D \quad (2)$$

$$\tau_2 = G_{\text{Al}} b \rho^{1/2} / 8\pi(1 - v) \quad (3)$$

where Φ is a constant, assumed to be equal to unity [26], G_{Al} is the shear modulus for the aluminum (26 GPa), b is

the modulus of the Burgers vector of dislocations, ρ is the dislocation density, v is Poisson's ratio (0.33 for aluminum), and γ_{gb} is the specific energy of grain boundary.

The equilibrium between the two stresses defines a critical dislocation density ρ_{cr} which is given by Eq. 4

$$\rho_{\text{cr}} = \gamma_{\text{gb}}^2 [26.4\pi(1 - v)]^2 / D^2 G_{\text{Al}}^2 b^2 \quad (4)$$

If $\rho < \rho_{\text{cr}}$, crystallites can grow. Contrarily, if the $\rho > \rho_{\text{cr}}$, they cannot grow until the exceeding dislocation density has been removed.

The critical dislocation density was calculated, using two different values of the specific grain boundary energy: 0.18 and 0.32 J/m². These two values were reported by Zhang et al. [28] as the extremes of γ_{gb} describing the dependence on the mismatch angle between grains. Results are reported in Table 2 and compared to the dislocation density in the nanometric grains of the five granulometric fractions of the cryomilled powder.

Independently on the specific grain boundary energy considered, the critical dislocation density is higher than the actual dislocation density. It might be concluded that the lattice strain is too low to stabilize the nanostructure, and consequently crystallite could grow immediately when heated. However, other stabilizing mechanisms not correlated to the density of dislocation have to be active.

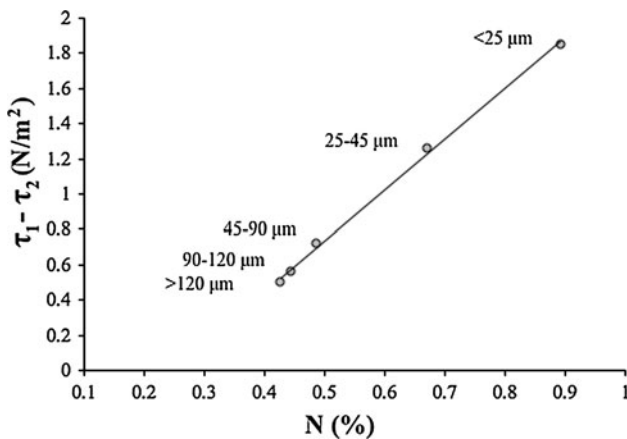
The two stresses τ_1 and τ_2 were calculated for the five granulometric classes, and results are reported in Table 3. They decrease on increasing the crystallite size, but τ_1 is around one order of magnitude higher than τ_2 .

The difference between the two stresses, which is also reported in Table 3, is a measure of the forces opposing grain growth not related to the dislocation density, i.e., the drag stress exerted by segregated impurities, grain boundaries particles and pores. It also decreases with increasing the crystallite size, and confirms the results reported in Fig. 6. The balance between stresses driving grain growth and stresses opposing it confirms that, for a micromechanics point of view, the smaller the crystallite size, the more stable the nanostructure on heating.

As reported extensively in literature [29–32], the grain growth is strongly inhibited by the pinning effect due to the presence of a second-phase particles. For the aluminum cryomilled powders it is reasonable to assume the

Table 3 Shear stresses acting on the grain boundary of the as-milled powder

Granulometric class (μm)	D (nm)	τ_1 (N/m^2) $\gamma_{\text{gb}} = 0.18 \text{ J}/\text{m}^2$	τ_1 (N/m^2) $\gamma_{\text{gb}} = 0.32 \text{ J}/\text{m}^2$	τ_2 (N/m^2)	$\tau_1 - \tau_2$ (N/m^2) $\gamma_{\text{gb}} = 0.18 \text{ J}/\text{m}^2$	$\tau_1 - \tau_2$ (N/m^2) $\gamma_{\text{gb}} = 0.32 \text{ J}/\text{m}^2$
<25	35 (1)	1.7×10^7	3.0×10^7	1.15×10^7	0.55×10^7	1.85×10^7
25–45	48 (2)	1.2×10^7	2.2×10^7	0.94×10^7	0.26×10^7	1.26×10^7
45–90	80 (3)	0.74×10^7	1.3×10^7	0.58×10^7	0.16×10^7	0.72×10^7
90–120	108 (6)	0.55×10^7	0.98×10^7	0.42×10^7	0.13×10^7	0.56×10^7
>120	119 (6)	0.50×10^7	0.89×10^7	0.39×10^7	0.11×10^7	0.50×10^7

**Fig. 7** The force opposing grain growth not related to the dislocation density vs. nitrogen content for each granulometric fraction, after degassing at 350 °C

formation of AlN, Al_2O_3 , and Al-oxy-nitride phases as a consequence of the milling process and/or subsequent annealing. Here, the most probable impurity in cryomilled powders is nitrogen. It might segregate at the grain boundary as solute clusters, and cause precipitation of AlN nanoparticles between and within Al grains upon heating. Since the contamination of the powder during milling comes from the interaction between the Al particles and the milling media, the finer the particle size, the more surface can interact with nitrogen.

Figure 7 reports the nitrogen content versus the force opposing grain growth related to the presence of a second-phase particles and nanopores. As expected, the quantity of nitrogen increases with decreasing the particle size. The nitrogen content was measured, for each granulometric fraction, after degassing at 350 °C in high vacuum (10^{-5} mbar) in order to avoid as much as possible the gas incorporated onto the surface of the particles as a consequence of the cryomilling process.

To characterize more in detail the second-phase particles, the finer powder was consolidated at 600 °C by means of SPS with a heating rate of 100 °C/min. The bulk sample obtained was studied using transmission electron microscopy. Figure 8a shows a BF image documenting an

ultra-fine grain after grain growth in which the second-phase particles are clearly visible along the original grain boundaries. Figure 8b reports a nanostructured region in which nanopores at grain boundary are pointed by arrows. However, due to the difficulty to identify nanopores by TEM analysis, the characterization was done qualitatively. The electron diffraction analysis (Fig. 8c, d) gives the presence of hexagonal AlN and cubic γ - Al_2O_3 . However, Fe and Si are both major impurities in commercial pure Al and also, the stainless steel balls used during cryomilling could constitute source of impurities. For this reason, the phase identification performed using SAED pattern could give only a partial picture of the second-phase particles that are present in the material.

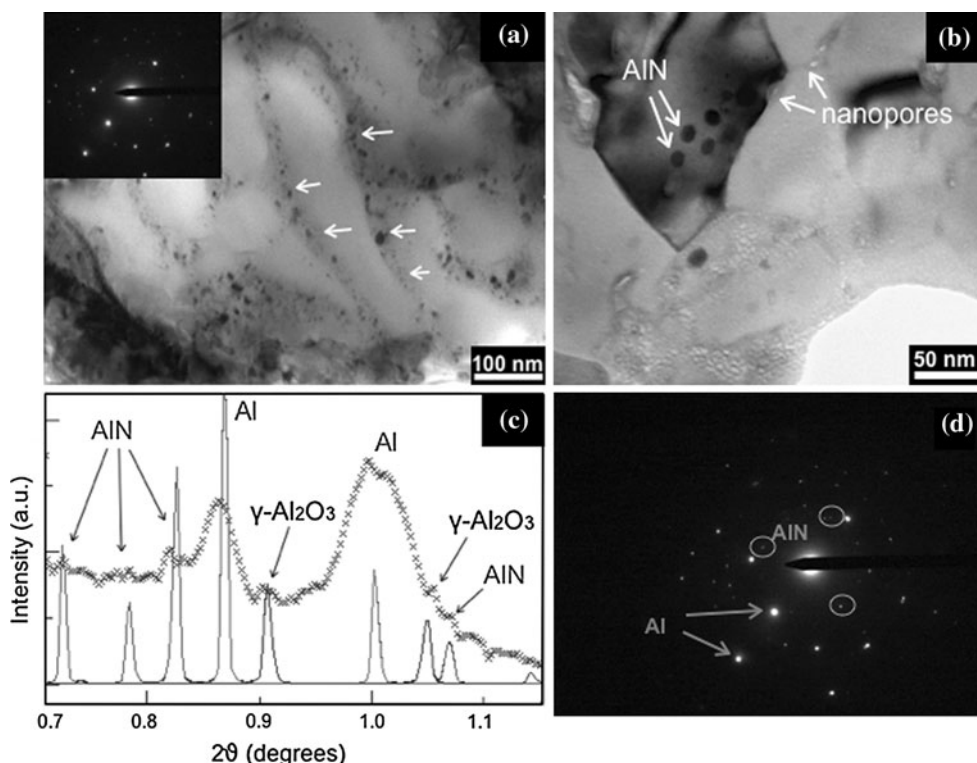
Grain growth of a 26 nm aluminum has been investigated by Zhou et al. [13]. Growth is very limited up to 450 °C, without any appreciable effect concerning the holding time; over this temperature, substantial time dependent grain growth occurs. This means that below 450 °C grain boundaries pinning forces are active, resulting in a grain growth exponent lower than 0.5. Zhou and co-workers conclude that nanostructured Al is stable up to homologous temperatures as high as 0.78, because of the effect of the solute drag, pore drag, second particles drag. Among the powders investigated here only the two finest follow the trend reported by Zhou. The resistance to grain growth decreases on increasing the initial grain size (Fig. 7).

As already mentioned by Witkin and Lavernia [1], our results confirm that while Al_2O_3 particles might be due to the presence of the oxide layer that covers the Al powder particles before milling (as proven by Salem and Sadek [32]), the formation of AlN is the result of milling in the liquid nitrogen environment. Both, Al_2O_3 and AlN are the major source of second-phase particle that act as pinning agents to enhance the thermal stability.

Conclusion

A nanostructured Al powder was obtained using cryogenic mechanical milling. The powder produced after

Fig. 8 TEM bright field images (**a**, **b**) and selected area electron diffraction (inset, **d**) on the consolidated SPS aluminum powder. Only the finer granulometric fraction (<25 μm) was used. Phase identification reported in **c** shows the presence of hexagonal AlN and cubic γ -Al₂O₃. Nanopores are clearly visible in **b**



25 h of milling in liquid nitrogen shows a broad distribution of the particle size, ranging from a few micrometers up to 150 μm . The microstructural characteristics of the five different granulometric classes of powder, as well as the thermal stability were investigated using ex situ X-ray diffraction and transmission electron microscopy. The trend shown by the powders on decreasing the particle size is very similar to that observed by Tian and Atzon on increasing the milling time. Therefore, the microstructural evolution of the powder during milling could be studied performing one single milling experiment, investigating the microstructure as a function of the particle size.

The crystallite size and the microstrain in the cryomilled powder are correlated to the size of the particles: the finer the particle size, the finer the crystallite size, and the larger the microstrain. This is expected to have a noticeable effect on the thermal stability of the nanostructured material. The driving force for the grain growth depends on the specific grain boundary surface area, and the microstrain offers a resistance to the grain boundary mobility during grain growth. However, additional phenomena concur to define the thermal stability of nanostructured Al obtained by cryomilling, as the drag stress exerted by grain boundary impurities, second-phase particles, and nanopores.

Acknowledgement Authors are grateful to Dr. Mario Zadra, K4Sint Srl, for the production of the sintered specimens.

References

1. Witkin DB, Lavernia EJ (2006) Prog Mater Sci 51:1
2. Zhou F, Witkin D, Nutt SR, Lavernia EJ (2004) Mater Sci Eng A 375–377:917
3. Lonardelli I, Almer J, Ischia G, Menapace C, Molinari A (2009) Scr Mater 60:520
4. Lee Z, Witkin DB, Radmilovic V, Lavernia EJ, Nutt SR (2005) Mater Sci Eng A 410–411:462
5. Jia D, Wang YM, Ramesh KT, Ma E, Zhu YT, Valiev RZ (2001) Appl Phys Lett 79:611
6. Han BQ, Huang JY, Zhu YT, Lavernia EJ (2006) Scr Mater 54:1175
7. Wang Y, Chen M, Zhou F, Ma E (2002) Nature 419:912
8. Han BO, Lee Z, Witkin D, Nutt S, Lavernia EJ (2005) Metall Mater Trans A 36:957
9. Hayes RW, Berbon PB, Mishra RS (2004) Metall Mater Trans A 35:3855
10. Shvindlerman LS, Gottstein G (2004) Z Metallk 95:239
11. Novikov VY (2006) Scr Mater 55:243
12. Malow TR, Koch CC (1997) Acta Mater 45:2177
13. Zhou F, Lee J, Dallek S, Lavernia EJ (2001) J Mater Res 16:3451
14. Moelle CH, Fecht HJ (1995) Nanostruct Mater 6:421
15. Lutterotti L, Matthies S, Wenk HR, Shultz AS, Richardson JW (1997) J Appl Phys 81:594
16. Lonardelli I, Wenk HR, Lutterotti L, Goodwin M (2005) J Synchrotron Radiat 12:354
17. Menapace C, Lonardelli I, Tait M, Molinari A (2009) Mater Sci Eng A 517:1
18. Popa NC (1998) J Appl Cryst 31:176
19. Eckert J, Holzer JC, Krill CE, Johnson WL (1992) J Mater Res 7:1751
20. Mohamed FA (2003) Acta Mater 51:4107
21. Criado JM, Gonzales M, Real C (1986) J Mater Sci Lett 5:467

22. Tian HH, Atzon M (1999) *Acta Mater* 47(4):1255
23. Revesz A, Ungar T, Borbely A, Lendvai J (1996) *Nanostruct Mater* 7:779
24. Zhao YH, Sheng HW, Lu K (2001) *Acta Mater* 49:365
25. Mukherjee P, Sarkar A, Barat P, Bandyopadhyay SK, Sen P, Chattopadhyay SK, Chatterjee P, Chatterjee SK, Mitra MK (2004) *Acta Mater* 52:5687
26. Chatterjee S, Wang HS, Yang JR, Bhadeshia HKDH (2006) *Mater Sci Technol* 22(6):641
27. Libardi S, Leoni M, Facchini L, D'Incau M, Scardi P, Molinari A (2007) *Mater Sci Eng A* 445–446:244
28. Zhang H, Upmanyu M, Srolovitz DJ (2005) *Acta Mater* 53:79
29. Song K, Aindow M (2008) *Mater Sci Eng A* 479:365
30. De Castro CL, Mitchell BS (2005) *Mater Sci Eng A* 396:124
31. Lavernia EJ, Han BQ, Schoenung JM (2008) *Mater Sci Eng A* 493:207
32. Salem HG, Sadek AA (2010) *JMEPEG* 19:356